The Astrophysical Journal Supplement Series, 272:12 (13pp), 2024 May https://doi.org/10.3847/1538-4365/ad34d8

Design and Performance of a 30/40 GHz Diplexed Focal Plane for the BICEP Array

Corwin Shiu[1], Ahmed Soliman[2,3], Roger O'Brient[2,3], Bryan Steinbach[2], James J. Bock[2,3], Clifford F. Frez[3], William C. Jones[1], Krikor. G. Megerian[3], Lorenzo Moncelsi[2], Alessandro Schillaci[2], Anthony D. Turner[3], Alexis C. Weber[3], Cheng Zhang[2], and Silvia Zhang[2]
[1] Princeton University, Princeton, NJ 08544, USA
[2] California Institute of Technology, Pasadena, CA 91125, USA
[3] Jet Propulsion Laboratory, Pasadena, CA 91109, USA
Received 2024 January 27; revised 2024 March 4; accepted 2024 March 15; published 2024 April 29

Abstract

We demonstrate a wideband diplexed focal plane suitable for observing low-frequency foregrounds that are important for cosmic microwave background polarimetry. The antenna elements are composed of slotted bowtie antennas with 60% bandwidth that can be partitioned into two bands. Each pixel is composed of two interleaved 12×12 pairs of linearly polarized antenna elements forming a phased array, designed to synthesize a symmetric beam with no need for focusing optics. The signal from each antenna element is captured in-phase and uniformly weighted by a microstrip summing tree. The antenna signal is diplexed into two bands through the use of two complementary, six-pole Butterworth filters. This filter architecture ensures a contiguous impedance match at all frequencies, and thereby achieves minimal reflection loss between both bands. Subsequently, out-of-band rejection is increased with a bandpass filter and the signal is then deposited on a transition-edge sensor bolometer island. We demonstrate the performance of this focal plane with two distinct bands, 30 and 40 GHz, each with a bandwidth of ∼20 and 15 GHz, respectively. The unequal bandwidths between the two bands are caused by an unintentional shift in diplexer frequency from its design values. The end-to-end optical efficiency of these detectors is relatively modest, at 20%–30%, with an efficiency loss due to an unknown impedance mismatch in the summing tree. Far-field beam maps show good optical characteristics, with edge pixels having no more than ∼5% ellipticity and ∼10%–15% peak-to-peak differences for A–B polarization pairs.

Unified Astronomy Thesaurus concepts: Astronomical instrumentation (799); CMBR detectors (259); Polarimeters (1277)

1. Introduction

Measurements of the spatial anisotropies of the cosmic microwave background (CMB) provide fundamental tests of cosmological theories. Measurements of a cosmological, degree-scale, B-mode polarization would provide a constraint on the tensor-to-scalar ratio r and place limits on the energy scale of inflation (Seljak & Zaldarriaga 1997; Kamionkowski & Jaffe 2001). The BICEP experiment has placed the tightest constraints on r, with an upper limit of $r_{0.05} < 0.036$ at 95% confidence (Ade et al. 2021).

These measurements are complicated by the fact that cosmological signals at large angular scales are highly contaminated by astrophysical foregrounds. Thermal emission from spinning dust grains produces a polarized emission that dominates at high frequencies (Finkbeiner et al. 1999; Planck Collaboration et al. 2020). Galactic synchrotron emission is emitted by electrons gyrating in magnetic fields and dominates at low frequencies (Ginzburg 1969; Bennett et al. 2013). CMB polarimetry experiments must have several frequency bands to remove contamination from foreground emission and uncover the underlying cosmological signal (Brandt et al. 1994).

Much remains to be learned about characterizing low-frequency foregrounds' spectral and spatial behaviors (Planck Collaboration et al. 2016). WMAP has observed substantial amounts of polarized foreground emission due to synchrotron radiation, even at high Galactic latitudes (Page et al. 2007), and this has been confirmed by other experiments (Krachmalnicoff et al. 2018; Eimer et al. 2024). Kogut et al. (2007) have observed a flattening of the synchrotron spectral index closer to the Galactic plane; however, Choi & Page (2015) have attributed this effect to the spatial correlation of dust and synchrotron.

A cross-correlation analysis of BICEP 95 and 150 GHz data up to 2018, when combined with publicly available WMAP K +Ka bands and Planck NPIPE 30 and 44 GHz data, did not yield any statistically significant evidence supporting the detection of synchrotron radiation (Ade et al. 2021). Therefore, while synchrotron contamination is not a driving source of uncertainty for current upper limits on r, as experiments become more sensitive, this foreground will play a more significant role in an unbiased recovery of r.

Furthermore, although synchrotron radiation is the primary source of low-frequency, polarized foregrounds, it may not be the exclusive source of low-frequency contamination. Magnetic dipole emissions resulting from thermal fluctuations of ferromagnetic interstellar grains have been proposed (Draine & Lazarian 1999; Draine & Hensley 2013). These emissions are expected to primarily occur $\nu \leqslant 100$ GHz, but the behavior likely differs depending on whether they are from iron inclusions in dust grains or free-flying iron nanoparticles (Hoang & Lazarian 2016). While there is currently no statistically significant detection of polarized anomalous microwave emission (AME; Planck Collaboration et al. 2016; Herman et al. 2023), increasingly precise measurements have the potential to improve the understanding of low-frequency foregrounds.

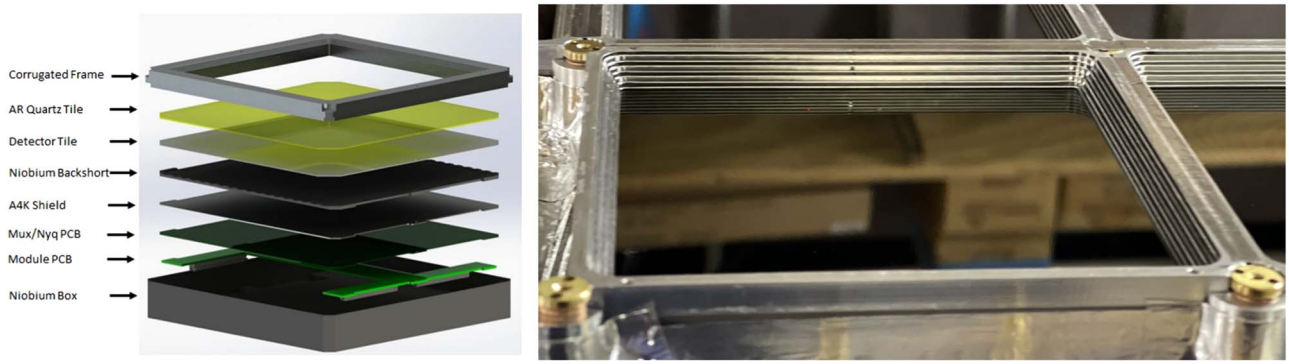

Figure 1. (Left) A cross-sectional 3D render of the focal plane module. The focal plane module consists of a detector tile hybridized with its readout chain, all housed in a superconducting niobium box and frame for magnetic shielding. (Right) A photograph of the machined corrugated frames designed to minimize undesired electrical interactions between the edge-pixel antenna elements and the structure. The visible tile is the antireflection coating, facilitating the backside illumination of the detectors through the silicon.

Advances in millimeter- and submillimeter-wave bolometer arrays directly drive improvements in characterizing the millimeter-wave sky. Ground-based CMB experiments have long been limited by photon noise (Ade et al. 2014), and therefore the sensitivity of an experiment scales with the square root of the number of detectors on the sky. For a given optical system and fixed focal plane area, the sensitivity would be improved by taking advantage of a wide-bandwidth antenna partitioned into multiple spectral bands. Various technologies exist to couple electromagnetic radiation onto bolometer arrays ranging from lenslet-coupled broadband sinuous antennas to multichroic horn antennas (McMahon et al. 2012; O'Brient et al. 2013). Several experiments have successfully deployed multichroic detector arrays, including ACT (Thornton et al. 2016) and SPT (Benson et al. 2014), and future-generation experiments will all be multichroic (Suzuki et al. 2016; Kiuchi et al. 2020; Walker et al. 2020).

This paper describes the design and performance of a fully lithographed, diplexed, low-frequency focal plane that will be powerful for characterizing synchrotron emission. The design builds upon previous BICEP instruments' successful phased array design (BICEP2 Collaboration et al. 2015). The phased array configuration gives us several advantages. The detectors are entirely planar and fully lithographed in thin films, which significantly simplifies the fabrication of these devices. The phased array configuration naturally synthesizes the beam without any need for focusing optics.

Antenna arrays have flexibility in their illumination pattern and can match feedhorn arrays' aperture efficiencies of $\sim$0.70, at smaller pixel sizes than their feedhorn counterparts (Griffin et al. 2002). Consequently, pixel densities from antenna arrays can be higher, owing to both geometric tiling of square pixels and an increased number of detectors within the same focal plane area. These theoretical advantages in efficiency arise from the ability for antenna arrays to have greater directivity. An extended discussion can be found in Appendix C, which outlines the theoretical contributions to focal plane mapping speed.

2. Focal Plane Overview

Our detector design is entirely planar and requires no contacting optics such as lenslets or horn antennas. Incoming optical power is coupled to polarized planar antenna arrays, the details of which are provided in Section 2.3. The power is then directed through a microstrip summing network, as explained in Section 2.4. The power subsequently passes through on-chip band-defining filters, which partition the power by frequency; the design of these filters is elaborated upon in Section 2.5. Finally, the energy is dissipated on a bolometer island and detected by a superconducting transition-edge sensor (TES; Irwin & Hilton 2005), the design of which is explained in Section 2.6. Variations in the TES current are read out by a time-domain multiplexing system based on SQUIDS (de Korte et al. 2003).

2.1. Overview of Detector Wafer

The Microdevices Laboratory at the Jet Propulsion Laboratory (JPL) fabricates the detector wafers, with a schematic of the detector module shown in Figure 1. Antenna arrays are built on 6 inch, 625 μm thick silicon wafers ($\epsilon_r = 11.8$). The millimeter wave circuit consists of four distinct layers, described in order from the layer closest to the silicon to the layer farthest away. First, a niobium ground-plane film is deposited, and then slotted antenna arrays are patterned through a liftoff process. Subsequently, we grow a 0.3 μm SiO_2 inner-layer dielectric (ILD) on top. Following that, we define the resistive termination for the bolometers. Finally, in the last film, we pattern the upper niobium conductor, which is responsible for shaping the antenna feed network and in-line filters. Fabrication details can be found in BICEP2 Collaboration et al. (2015). Figure 2 shows a photograph of the antenna elements.

Because the antenna arrays are backside illuminated, a fused-quartz ($\epsilon_r = 3.9$) antireflection layer is applied to the bottom of the entire stack, serving as the topmost layer facing the sky. As a result, the antenna elements face a superconducting niobium reflective backshort, positioned at a distance of $\lambda/4$ away. The entire detector module comprises the quartz antireflection wafer, silicon detector array, niobium backshort, amumetal 4k magnetic shielding, and readout printed circuit board cards, all enclosed in a compact niobium frame. Additional information on the focal plane engineering, measurements, and hybridization can be found in other publications (Schillaci et al. 2023; Soliman 2023).

2.2. Mitigating Polarized Frame-edge Effects

Unwanted electromagnetic interactions between the niobium frame and antennas degrade the quality of the antenna beams.

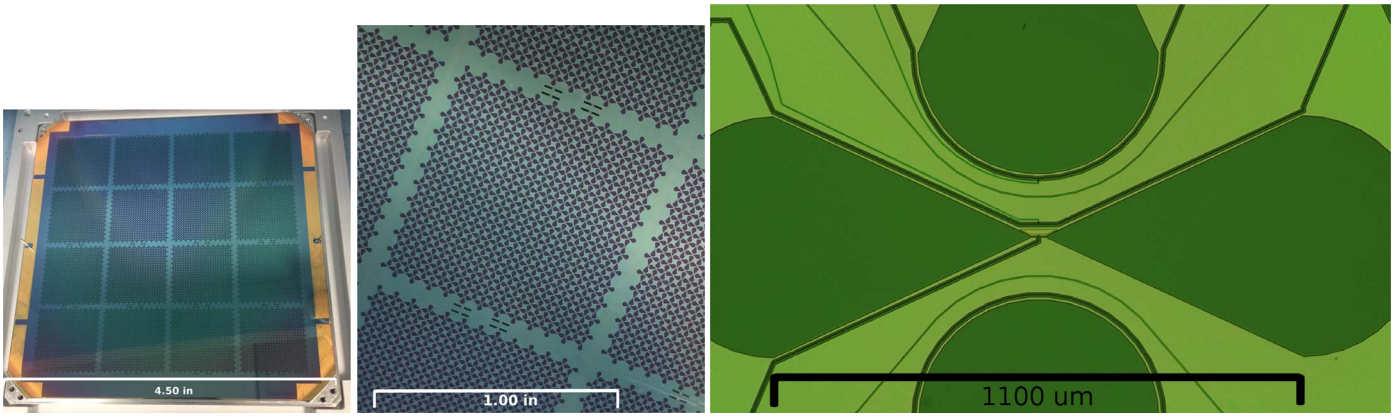

Figure 2. Bowtie tile. (a) Photograph of a full tile showing a 4 × 4 grid of pixels. (b) Zoom-in on a pixel. We have a 12 × 12 pairs of bowtie antennas comprising the antenna array with four bolometers capturing A/B polarization at our two bands. (c) Zoom-in on a single antenna element. Dark green indicates the ground-plane cutout showing both the subantenna and the coplanar waveguide driving the antenna.

Employing a solid metal frame can lead to polarization-dependent deformations of the antenna beams, especially for edge pixels. Such deformations can introduce (1) differential beam centers for orthogonal polarizations and result in dipole artifacts or (2) polarized beam ellipticities and result in quadrupole artifacts. These beam systematics leak temperature to polarization and potentially introduce a false B-mode signal (Hu et al. 2003; Ade et al. 2015). Although BICEP has developed a deprojection technique to mitigate low-order beam systematics effectively, controlling higher-order beam effects is challenging (Ade et al. 2016).

At lower frequencies, there are far more edge pixels than center pixels. Soliman et al. (2020) has devised a novel corrugated frame that minimizes polarized beam steering. These grooves serve to smooth out impedance discontinuities, effectively reducing the abrupt boundaries caused by the presence of a conductive frame. The frame relies on quarter-wave corrugations with quarter-wave pitches. This design ensures that surface waves reflecting off the corrugated frame become out of phase and destructively interfere. To account for the wide bandwidth of this antenna, Soliman (2023) designed a doubly corrugated frame with depths tailored for both 30 and 40 GHz. The peak-to-peak polarization subtraction for the broadband corrugated frame shows a minimized differential offset (<10%–15%). The remaining residuals are effectively filtered out using a deprojection technique developed by the BICEP team. These results show that the corrugated frame successfully minimizes the differential offset compared to earlier focal plane unit detector designs; Ade et al. (2019) report a differential offset of ∼40%. Readers interested in the design specifications of this corrugated frame are referred to a different publication (Soliman 2023).

2.3. Antenna Design

A single pixel consists of two interleaved phased antenna arrays. To prevent grating lobes, a phased antenna array must be spaced to Nyquist sample the focal plane (Kuo et al. 2008). The antenna elements are arranged in a square lattice rotated by 45°, which sets the Nyquist condition as the following inequality:

$$s \leqslant \frac{\lambda_{0,\min}}{\sqrt{\epsilon_r}}\left(1 - \frac{1}{N}\right). \quad (1)$$

In this equation, s is the antenna spacing and $\lambda_{0,\min}$ represents the minimum operating wavelength of the band. The term in the parenthesis suppresses the array factor's end-fire beam response where N is the number of antenna elements along a single axis of the square lattice.

This relationship imposes an upper limit on the size of the antenna element, which must not exceed a wavelength. This constraint can be challenging because wideband antennas are typically larger structures spanning multiple wavelengths (Chu 1948). Another common strategy to achieve large bandwidths is designing self-complementary antennas, which have the property of frequency-independent input impedance (Mushiake 1992). This concept is the driving principle behind sinuous antennas, as detailed in O'Brient et al. (2008, 2010, 2013). However, this approach is not suitable for this architecture, because of the space requirements for including orthogonal antenna elements. Consequently, implementing this phased antenna array scheme necessitates designing an antenna with a broad first resonant peak, which is then operated in that mode. This is the fundamental principle behind this design. Like the slot dipole antenna, the slotted bowtie antenna is linearly polarized. This design incorporates a wide flare angle, which broadens the first resonance and increases the available bandwidth (Brown & Woodward 1952). While a bowtie antenna is sometimes described as a traveling wave antenna parameterized solely by its flare angle, this is not true for a finite antenna lacking a resistive termination. An impedance discontinuity leads to the formation of standing waves and therefore resonant modes. As discussed by Stutzman & Thiele (2012) as well as Balanis (2016), increasing the flare angle reduces the antenna's standing-wave characteristics by minimizing the phase mismatch between the voltage and currents along the slot. This results in a smoother impedance response and effectively widens the first resonance. This phenomenon is evident in full-field FEM simulations of the slotted bowtie antenna using Ansys High-Frequency Structure Simulator (HFSS). Figure 3 illustrates that an increase in flare angle shifts the first resonance to lower frequencies and smoother reactance variations.

Additionally, rounding out the ends of the slotted bowtie modestly reduces the driving-point impedance at no cost of space for our feed network (Qu & Ruan 2006). A flare angle of

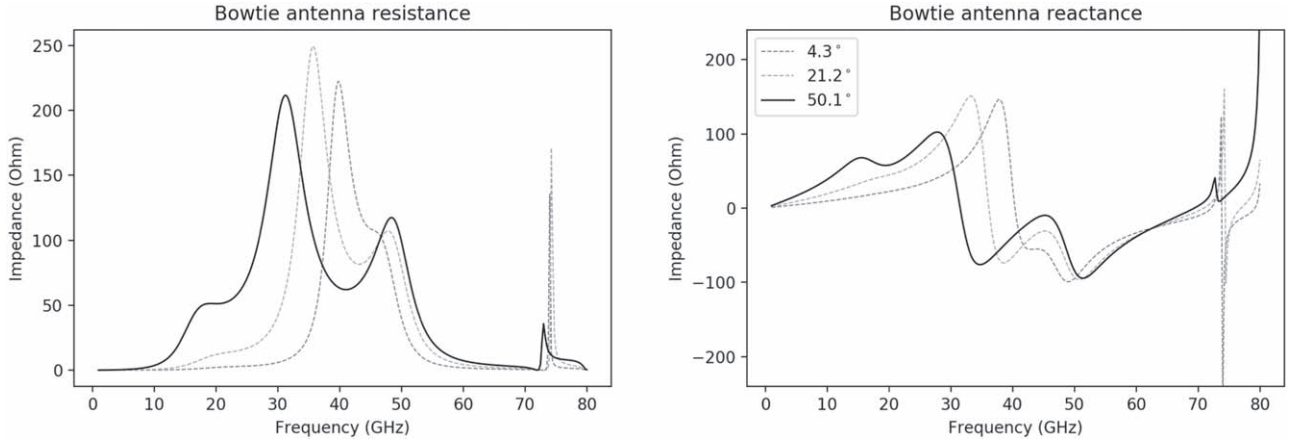

Figure 3. The simulated resistance and reactance of the bowtie antenna, calculated using Ansys HFSS. The simulation shows that the antenna reactance diminishes as the flare angle increases and the first resonance widens. The solid line, labeled with a flare angle of 50°, is the nominal configuration. We drive this antenna at 100 Ω using a quasi-CPW line in our design.

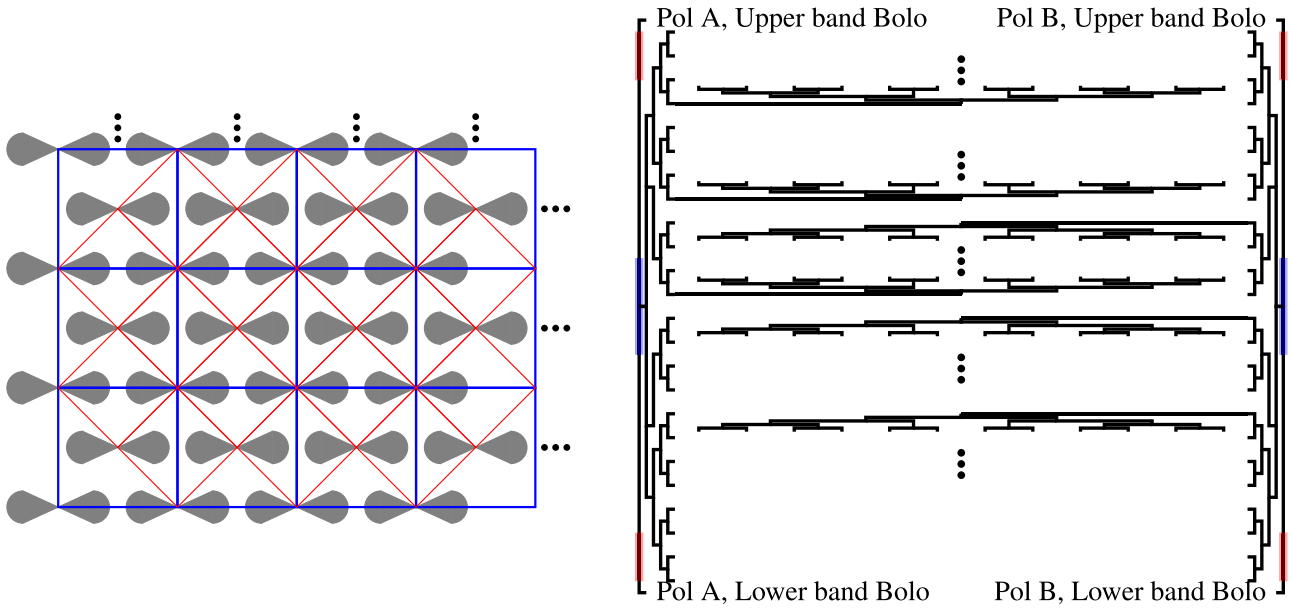

Figure 4. (Left) An abbreviated schematic of a single-polarization antenna array, depicted in two colors to illustrate two possible descriptions. The red array represents this design as a square array rotated by 45°, establishing the Nyquist criterion for antenna spacing. Alternatively, the blue array describes our configuration as a product of a square array with two elements per square, offering a convenient analytical description of the total beam. (Right) An abbreviated schematic of a single pixel's microstrip summing tree network. Antenna subelements are located at the ends of all horizontal brackets. Power is coherently summed by the horizontal network, and then summed by the vertical network. Different polarizations are directed left and right. The signal is partitioned by a diplexer, as depicted in blue, and filtered by a bandpass filter, as depicted in red, and terminated on a bolometer island.

50° was determined to meet our bandwidth requirements while still adhering to space constraints.

In this design, depicted on the left side of Figure 4, a pixel consists of a square lattice rotated by 45°, highlighted in red. The antenna spacing between nearest-neighbor elements is $s = 1315\ \mu$m. Although this spacing is ∼15% smaller than required by the Nyquist criterion (Equation (1)), we observed improved impedance characteristics with the smaller spacing.

However, a more convenient mathematical representation would be the array in blue: a single polarization consists of a 12×12 square grid of resonant bowtie antenna pairs. These pairs of antennas are arranged in a Bravais lattice with vectors $\vec{a} = (2a, 0)$, and $\vec{a}_2 = (0, 2a)$, where the lattice spacing is $a = 930\ \mu$m. Individual pairs are located at $\vec{a} = (0, 0)$ and $\vec{a} = (a, \pm a)$, with the sign originating from the polarization. This alternative parameterization of the lattice is useful for the beam model in a later discussion in Section 3.2. The lattice for the orthogonal polarization is achieved by a simple translation of $(a, 0)$.

2.4. Microstrip Feed Network

We collect power by combining signals from 12×12 bowtie pairs in the array with a microstrip feed network. All antennas are coherently fed with uniform power division. A cartoon diagram of a simplified microstrip network is shown by the right side of Figure 4. We achieve coherent summation by summing waves coherently by row and then as a column using microstrip T-junctions. The power is subsequently split by a diplexer and filtered before terminating onto a bolometer island.

We refer to uniform and in-phase summation as *top-hat* illumination. We chose top-hat illumination for its simplicity.

However, it is important to note that tapered illumination could improve beam quality (O'Brient et al. 2012), as top-hat illumination tends to result in larger side lobes.

A relatively high-impedance line of around $\sim 100\,\Omega$ is required to drive the bowtie antenna efficiently. This impedance is unachievable with microstrip lines with a thin ILD (0.3 μm of SiO_2). Instead, we can create a high-impedance line by removing the ground plane directly underneath the conductor, so that the field lines mimic those of a coplanar waveguide (CPW; Arbabi et al. 2006). We found that a substantial gap, 20 μm side-to-side, allowed us to achieve our desired impedance. Then, adjacent quasi-CPW lines join at a T-junction and transition, with minimal reflection loss, to a microstrip line for the remainder of the summing tree.

Furthermore, ground bridges are strategically placed to short the two outer ground conductors. These bridges eliminate potential slotline modes that may radiate. Their spacing has determined to ensure that no slotline modes are excited within the operating bandwidth of this detector array.

Crosstalk can be a concern with phased array antennas. Coupling between neighboring transmission lines can introduce phase errors across the pixel, leading to beam steering (BICEP2 Collaboration et al. 2015). The larger footprint of the bowtie antenna restricts the spacing available for routing the summing tree. We mitigate crosstalk by two design principles. First, we opt for a thin ILD to enhance the confinement of the field lines of the microstrip mode. Second, we route the microstrip lines to fan in and out wherever space allows. Coupling between microstrip lines relies on excitations of even and odd modes (Pozar 2005). By flaring the microstrip lines, no significant sections of the summing tree remain in close contact, and the two modes continually change impedances along the lines. This prevents coupling even when lines must compress within a few line widths of distance. The spacing of the antennas necessitates lines as close as 5 μm. However, these modes are confined within a thin ILD (0.3 μm) and remain in close proximity for no more than 500 μm, about 10% of a wavelength, resulting in minimal coupling. HFSS simulations show crosstalk levels of -50 dB between neighboring lines at our tightest junctions. We expect crosstalk to be a minor contributor to beam effects, with frame-edge coupling assuming the predominant role.

2.5. On-chip Filtering

Each detector band is synthesized from a combination of the diplexer and the wideband bandpass filter. The bandpass filter defines the upper-band edge for the high-frequency band and the lower-band edge for the low-frequency band. The diplexer splits the power contiguously between the two bands.

The diplexer is composed of a sixth-order high-pass and a low-pass Butterworth filter. In this topology, the specific values for all the components have been carefully selected to achieve equal and opposite reactance for the two inductance–capacitance (LC) ladder circuits. Therefore, the reactance is matched across all frequencies and identically cancels out at the antenna input, ensuring a continuous power split without any reflections. The design is described in detail in Matthaei et al. (1980). We chose this design for its simplicity and robustness to fabrication nonuniformity.

This circuit was realized by finding lithographic approximations to lumped-element circuit elements through extensive simulations using Sonnet. Lumped inductors are synthesized by subwavelength high-impedance transmission lines, while lumped capacitors are synthesized by parallel plate capacitors. In practice, lithographic elements only approximate lumped elements at microwave frequencies. Frequency dispersion reduces their effectiveness. We selected a three-pole Butterworth filter to strike a balance between achievable lithographic elements and filter sharpness. In particular, series capacitors become more dispersive with larger capacitance values, nullifying the benefits of higher-order filters.

Table 1
Circuit Design Table for On-Chip Filters

	L_1	C_1	L_2	C_2	L_3	C_3
Bandpass	1.85	0.25	2.70	0.41	⋯	0.51
Diplexer	1.55	1.76	1.55	1.20	0.758	0.259

Note. The corresponding circuit elements are in Figure 5. To scale from the design table to physical values: inductor values are scaled by $\omega_0^{-1}Z_0$, and capacitor values are scaled by $(\omega_0 Z_0)^{-1}$, where $\omega_0 = 2\pi f_0$ is the desired -3 dB transition between the two bands and Z_0 is the port impedance. For this particular design, $f_0 = 35GHz$ and $Z_0 = 25\Omega$. Simulations are then performed to convert the electrical inductance and capacitance to a lithographic element, the details of which are outlined in Appendix B.

The bandpass filter design concept was adapted from the previous BICEP style of filters (BICEP2 Collaboration et al. 2015). In its most basic description, the bandpass filter architecture consists of three-series LC tanks joined by impedance inverters (Matthaei et al. 1980). The Kuroda identities convert the impedance K-inverter into a physically realizable capacitor network (Pozar 2005). Additionally, we found it advantageous to perform a Y-to-π transformation of the capacitor network at these microwave frequencies to reduce the series capacitances necessary for lithography. The design table is tabulated in Table 1, accompanied by a corresponding circuit diagram in Figure 5. The left side of Figure 6 shows the simulated performance of these filters, and we leave the discussion of the performance to Section 3.1.

2.6. Bolometer Design

Power captured by the antennas propagates through the microstrip network, passes through on-chip filters, and is ultimately dissipated as heat by a lossy gold termination on a suspended bolometer island. This heat is ultimately detected by a TES bolometer (Irwin & Hilton 2005).

TES bolometers are widely adopted in many CMB experiments because they have excellent noise properties and are a suitable choice to make large-format arrays. They can be fabricated using standard thin-film lithography techniques, and importantly, they are compatible with multiplexing schemes (de Korte et al. 2003; Irwin & Lehnert 2004; Dobbs et al. 2012). Additionally, they have a strong negative electrothermal feedback, increasing the device's linearity (Irwin & Hilton 2005). A TES bolometer is operated by voltage biasing the detector between superconducting and normal states. When an incident photon is absorbed and heats the bolometer, slight temperature changes will result in significant variations in the TES resistance. The electrical current flowing through the device is inductively coupled to the SQUID readout scheme, enabling a highly sensitive measurement of relative energy changes.

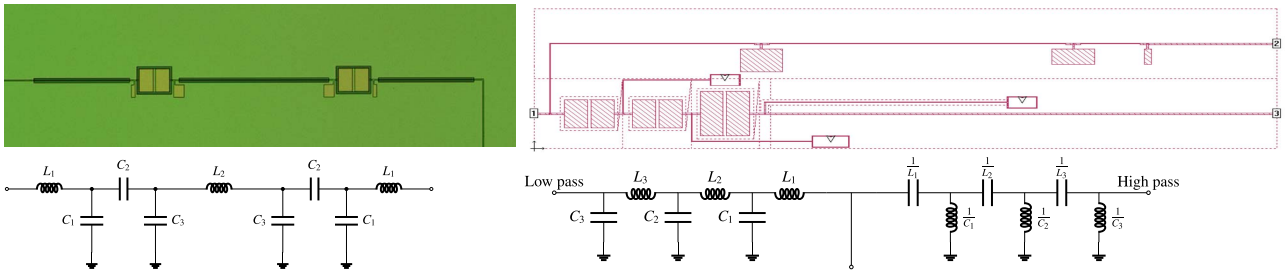

Figure 5. On-chip filters that define the bandpass of the detectors. On the left is the bandpass filter that defines the extremities of the bands. The bandpass filter is equivalent to a three-pole LC series resonator with impedance inverters. On the right is the diplexer composed of a Butterworth high-pass and low-pass filter. The image above is a Sonnet schematic of the diplexer, where port 1 connects to the antenna network, port 2 is the low passband, and port 3 is the high passband. Below the image is a lumped-element equivalent network for this diplexer. The design table is in Table 1, where the inductor values must be scaled by Z_0/ω_0 and capacitor values scaled by $(\omega_0 Z_0)^{-1}$.

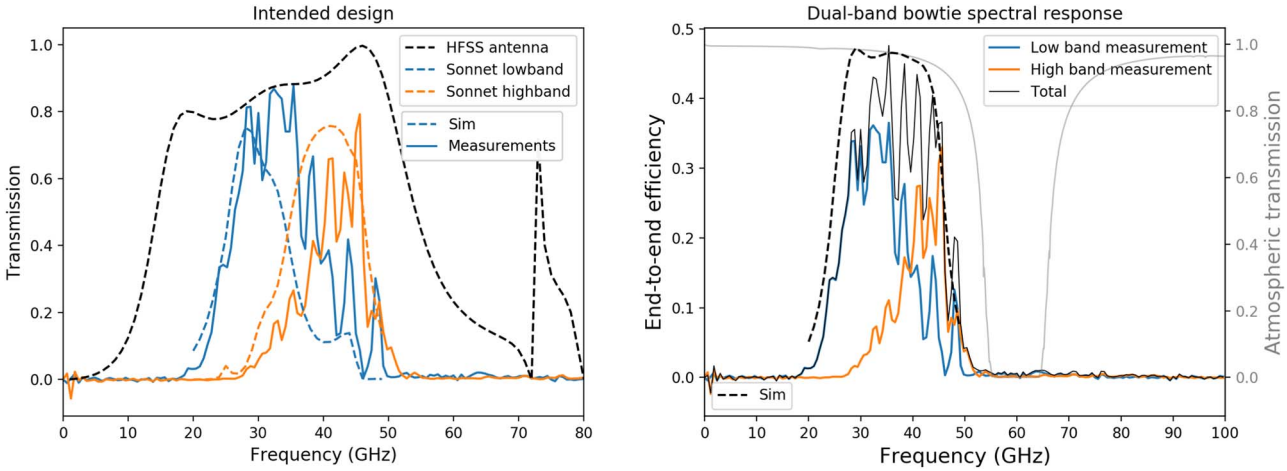

Figure 6. Comparison between the design spectrum (in the dashed lines) and measured spectrum (in solid lines). The left panel highlights the simulated spectra, while the right panel highlights the simulated spectra. (Left) Simulations of the antenna transmission spectrum and the intended bands from the on-chip filters. Measured spectra have been scaled vertically for visual comparison. A comparison of simulated and measured values shows that the diplexer shifted up 4 GHz from intended design values, causing the lower band to encroach on the bandwidth of the higher band. This leads to unequal bandwidths between the two bands. (Right) An unknown impedance step causes a ∼3 GHz ringing. The atmospheric transmission at the South Pole is shown in gray, with molecular oxygen responsible for the line at 60 GHz (Tretyakov et al. 2005).

The detector design has two TES in series with different superconducting transition temperatures (T_c). One is an aluminum TES with a $T_c = 1.2$ K. This TES is designed to handle significantly higher optical loading in laboratory settings, in particular during calibration and ground-based optical characterization. The titanium TES has a much lower $T_c = 450$ mK for science observation with significantly reduced loading conditions. This TES offers superior detector stability and substantially higher sensitivity. The saturation power is a key design parameter of a bolometer and is the total power needed to bring the TES temperature to T_c:

$$P_{\rm sat} = P(T_c) = G_c T_c \frac{1 - (T_{\rm bath}/T_c)^{(n+1)}}{n+1}, \quad (2)$$

where $T_{\rm bath} \sim 280$ mK is the surrounding heat bath temperature, G_c is thermal conductance of the bolometer isolation legs at $T = T_c$, and n corresponds to the nature of phonon transport in the legs. For our bolometer design, the isolation legs are thin, so phonons are reduced to two dimensions and n has been experimentally determined to be ∼2. G_c is carefully designed so that $P_{\rm sat}$ is above the optical loading we expect when doing science observations at the South Pole while keeping it as low as possible in order to minimize the noise-equivalent power (NEP).

The noise in the TES detector consists of several components, including photon noise, phonon noise, SQUID readout noise, and Johnson noise from the shunt resistor (Zmuidzinas 2003). The latter two sources of noise can be deliberately minimized to be subdominant to the first two, which are intrinsic and establish the fundamental sensitivity of the bolometer. Thermal fluctuations across the silicon nitride legs of the bolometers contribute the following NEP:

$$NEP^2_{\rm phonon} = 4k_B T_c^2 G_c F(T_c, T_{\rm bath}), \quad (3)$$

where $F(T_c, T_{\rm bath})$ is a function of bath and TES island temperature and accounts for the nonequilibrium effects (Mather 1982). Typical values for our bolometers are $F \sim 0.5$.

Because phonon NEP is proportional to the square root of thermal conductance, the value of G_c has a direct impact on mapping speed. The bolometer island is suspended by four legs, forming the weak thermal link between the island and the thermal bath. The G_c, tunable by leg lengths, is optimally designed to maximize detector sensitivity, while avoiding saturation during science operation. The bolometer legs are constructed from 1 μm thick low-stress nitride (LSN) and are 9 μm wide for the leg that bridges the wire connecting the microstrip summing tree to the resistive termination, 6 μm wide for the two legs that carry the DC bias lines, and 4 μm thick for

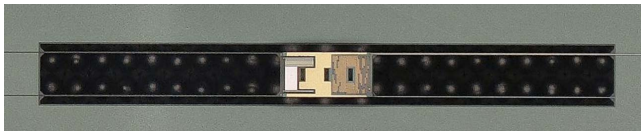

Bolometer Properties	G_c	T_c	R_n	P_{sat}
Median	14.8pW/K	428mK	101.9 mΩ	1.58pW
Standard Deviation	3.4pW/K	10mK	18.7mΩ	0.24pW

Figure 7. (Left) A microscope image of a suspended bolometer island on the detector wafer. In the photograph, on-sky power propagates from the upper right leg and is deposited on the lossy gold meander on the right side of the island. Two DC bias lines come in from the two left legs and bias the Al and Ti TES bolometers in series. (Right) A tabulation of measured bolometer properties.

the one remaining support leg. The legs are 800 μm long. Note that these differ from the G_c values used for the monochromatic 30/40 GHz bolometer arrays as described in other publications (Zheng et al. 2020; Zhang 2023). A tabulation of the bolometer properties and performance is shown in Figure 7. While detector sensitivity can be enhanced by reducing phonon noise with a lower $T_{\rm bath} = 100$ mK, the incremental gains are outweighed by the increased cryogenic complexity, given that these detectors are photon-noise limited. Consequently, a lower 100 mK design was not pursued (Zheng et al. 2020).

3. Optical Characterization

This focal plane was cooled down and tested in a testbed cryostat that mimics the filtering present on a BICEP-style receiver but lacks the imaging optics of the complete telescope insert. A series of optical filters, including absorbing plastic filters and reflective metal-mesh filters, was used to limit the radiative thermal load on the focal plane (Ade et al. 2006). The on-chip filtering ultimately defines the bands of the detectors for science observation. All laboratory measurements were performed using the aluminum superconducting transition designed for higher optical load.

To minimize radio-frequency interference (RFI), archival measurements were conducted at night with WiFi routers and personal wireless devices powered off. Laboratory testing has demonstrated that the majority of RFI for these styles of receivers couples in through the readout chain rather than the optical chain (Soliman 2023). To reduce RF pick-up, a Faraday cage made of 1/8 inch wire metal mesh enclosed the readout electronics and housekeeping electronics. Additionally, aluminized Mylar tape was used between readout modules for RF shielding.

3.1. Spectral Bandpass Characterization

The spectral response of these antennas, $S(\nu)$, was characterized using a Martin–Puplett Fourier transform spectrometer (FTS). The input light is generated by an HR-10 source submerged in liquid nitrogen for thermal stability of the source. First, the millimeter-wave radiation passes through a wire grid, selecting for linear polarization. Subsequently, it is directed to a collimating mirror and onto a beam splitter consisting of a wire grid oriented 45° to the incident polarization. The beam is split into two: one path is a fixed rooftop mirror, and the other is a variable rooftop mirror continuously driven by a stepper motor. The two paths interfere when returning to the beam splitter, reflecting off an output wire grid. This wire grid is oriented at 45° so that only the desired linear polarization leaves the FTS box, thereby cleaning up any undesired polarized systematics. Finally, the beam is focused by an HDPE lens designed to illuminate a single pixel in the optical testbed. We do not believe that this source is beam-filling, so the throughput on the single detector is expected to be $A\Omega = f\lambda^2$, where f is a fractional value. However, it is important to note that the FTS source operates in the Rayleigh–Jeans limit: $I(\nu) = k_b T \lambda^{-2}$. Therefore, the reported detector response $S(\nu)$ is equivalent to the response to a source with constant spectral radiance.

The spectral response of the detectors is defined in the band center by

$$\nu_0 \equiv \frac{\int \nu S(\nu)\, d\nu}{\int S(\nu)\, d\nu} \tag{4}$$

and bandwidth by

$$\Delta\nu \equiv \frac{\left(\int S(\nu)\, d\nu\right)^2}{\int (S(\nu))^2\, d\nu}. \tag{5}$$

The normalization of our spectra was computed by measuring the optical response of our detectors. This was performed by comparing the optical loading of the detectors under a beam-filling blackbody source at room temperature and at liquid nitrogen temperatures. Therefore, the spectra in Figure 6 represent the end-to-end optical efficiency of the antennas to in-band photons, accounting for losses through the optical elements such as the window and millimeter-wave filters, as well as electrical losses through impedance mismatches and dielectric loss in the microstrip summing tree.

The left side of Figure 6 shows the simulated antenna bandwidth as the dashed black line, along with simulated on-chip filters defining the two bands. The simulated antenna spectrum suggests additional usable bandwidth; however, the oxygen line at 60 GHz must be rejected using on-chip filters. The diplexer continuously distributes power between the two bands. There is spillover between the two bands, as the filter is optimized to minimize reflected power between the bands rather than band separation. This design choice was made for two reasons: (1) avoiding power loss between the two bands, as there are no atmospheric lines between 30 and 40 GHz, and (2) opting for a conservative filtering scheme. This design avoids reliance on two electrically interacting on-chip filters, where drift in one would interfere with the other through three-port interactions. Ultimately, this spectral spillover reduces our lever arm in measuring β_s, as the effective frequency centers of both bands are closer in frequency space.

The right side of Figure 6 shows the full focal plane averaged spectrum of both bands in blue and orange. The sum of the two bands is the solid black line, indicating that physical measurements show a consistent bandwidth between measurements and our simulated expectations. Tabulated band centers and widths are in Table 2. High fractional bandwidth is achieved, with both the high and low bands having substantially larger fractional bandwidth than the traditional slot design (Zheng et al. 2020).

Power is split between the two contiguous channels, indicating that the diplexer performs as intended. The upper-

Table 2
Summary Statistics of the Optical Performance of the Diplexed Focal Plane

	Spectra			Beams		
	ν_0	$\Delta\nu$	$\frac{\nu_0}{\Delta\nu}$	FWHM$_M$ (deg)	FWHM$_m$ (deg)	$\Delta(M-m)$ (deg)
Low Band	33.7 GHz	21.2 GHz	63%	18.5 ± 1.3	16.9 ± 0.9	1.6 ± 1.2
High Band	41.5 GHz	15.4 GHz	37%	15.1 ± 1.6	14.1 ± 1.4	0.8 ± 0.4

Note. A shift in the diplexer central frequency has caused spillover of the lower-band bandpass, encroaching on the bandwidth of the upper band. The beam-ellipticity statistics are driven by undesired polarized frame and edge-pixel electromagnetic interaction, which make up the majority of the pixels on a 4×4 focal plane. Notably, center pixels and edge pixels with the orthogonal polarization to the frame, show significant improvements to their beam ellipticities.

and lower-band edges agree with our simulated results. The diplexer appears to have shifted from the design frequency by 10%, which causes more spillover from the lower band to the upper band than intended.

The achieved optical efficiency is modest, with end-to-end measurements of 20%–30% optical efficiency. A portion of these quoted lower optical efficiencies occurs due to spectral spillover; a sum of the bands shows 35% efficiency in the passband. While this efficiency remains lower than the monochromatic slot design, these detectors remain competitive, with similar optical responsivity, due to larger overall bandwidth.

Additionally, there is an observed ∼3 GHz ringing in the frequency bands, suggesting the presence of an impedance mismatch associated with this length scale or one of its harmonics. The effective dielectric constant of microstrip modes in a 0.3 μm SiO_2 is approximately $\epsilon_{\mathrm{MS,\ eff}} \sim 3.4$, which results in a corresponding wavelength of ∼54 mm. Unfortunately, many possible junctions within the summing tree have this length scale, making it challenging to identify the source of this impedance mismatch.

In future iterations of this design, we would adjust the diplexer to shift the frequency down so that the two bands have a more balanced distribution. Alternatively, we can employ a different filtering scheme to achieve a sharper separation between the two bands, at the expense of some loss of photons between the two bands. A preliminary design has been explored in Appendix A. Additionally, more investigative work must be done to identify the source of impedance mismatches in the microstrip network, to identify the source of reflections. Highlighting that this design meets the baseline requirement within BICEP Array to achieve its science goals, there remains significant potential for enhancing the end-to-end efficiency of these detectors to meet simulated expectations.

3.2. Far-field Beam Patterns

The antenna beam of a phased antenna array is, in principle, highly tunable. The configuration of the radiators, along with the amplitude and phase applied to each antenna element, collectively determine the beam shape. The gain of an antenna array is modeled as the following:

$$G_{\mathrm{array}}(\theta, \phi) = G_0(\theta, \phi)|AF(\theta, \phi)|^2, \tag{6}$$

where G_0 is the gain of an individual element, and AF is short for the array factor. The array factor is the discrete Fourier transform of the antenna elements. Generically, the array factor can be expressed as $AF(\theta, \phi) = \sum_{n,m} A_{nm} \exp\left(i\frac{2\pi}{\lambda}\hat{r} \cdot \vec{x}(n, m)\right)$, where $\hat{r} = \sin\theta\cos\phi\hat{x} + \sin\theta\sin\phi\hat{y}$, where θ and ϕ are the polar and azimuthal angles, respectively, A_{nm} is the excitation amplitude of each radiator, and $\vec{x}(n, m)$ is the location of each radiator.

The number of subradiators was chosen to match the telescope optics of f/1.5 in BICEP Array (Hui et al. 2018), but in principle, this can be tunable to any optical system. For a single polarization, a pixel comprises of a 12×12 square grid of resonant bowtie antenna pairs. This parameterization is convenient, as it allows us to analytically separate the array factor into the product of two array factors:

$$|AF(\theta, \phi)| = \frac{\sin\left(\frac{2\pi Ma}{\lambda}\sin\theta\cos\phi\right)\sin\left(\frac{2\pi Ma}{\lambda}\sin\theta\sin\phi\right)}{M^2\sin\left(\frac{2\pi a}{\lambda}\sin\theta\cos\phi\right)\sin\left(\frac{2\pi a}{\lambda}\sin\theta\sin\phi\right)} \times \cos\left(\frac{2\pi}{\lambda}\frac{a}{2}\sin\theta(\cos\phi \pm \sin\phi)\right). \tag{7}$$

The first term represents the $M = 12$ square array factor. The second term represents the two-element antenna pair, with the $\pm$ for the A and B polarizations respectively. The sign choice originates from antenna pairs being located at quadrants 1 and 3 for polarization A and quadrants 2 and 4 for polarization B. This beam model implies an inherent A–B mismatch between the two polarization pairs, arising from the two-element component portion of the array factor. Indeed, the A–B mismatch for this component increases with larger polar angles from the antenna boresight. However, the square array factor concentrates the antenna beam and minimizes this source of A–B mismatch. A calculation shows that, for a 12×12 array, this pairwise array factor contributes only a 0.7% peak-to-peak A–B mismatch. The intrinsic antenna element beam, G_0, is determined through HFSS simulations and contributes an additional 2%, leading to a theoretical limit of a 2.7% peak-to-peak A–B mismatch.

Previous antenna arrays have used an 8×8 array. This is expected to have a 1.6% peak-to-peak A–B mismatch purely from the pairwise array factor, and a 5% peak-to-peak A–B mismatch when accounting for individual beams. The increased number of elements for this antenna array design suppresses differential ellipiticity and leads to overall better beam performance.

Far-field beams were characterized by an in-house beam mapper, which consists of a Thorlabs MC2000 optical chopper: a variably controlled (2–20 Hz) thermally chopped source that is mounted on an X–Y translation stage. The thermal source is a heated ceramic, reaching temperatures of several hundreds of degrees Celsius, and is chopped with respect to a reflective room-temperature blade. The reflected beams terminate within the cold optics of the testbed. To prevent multiple reflections in our measurement setup, we took care to blacken the beam

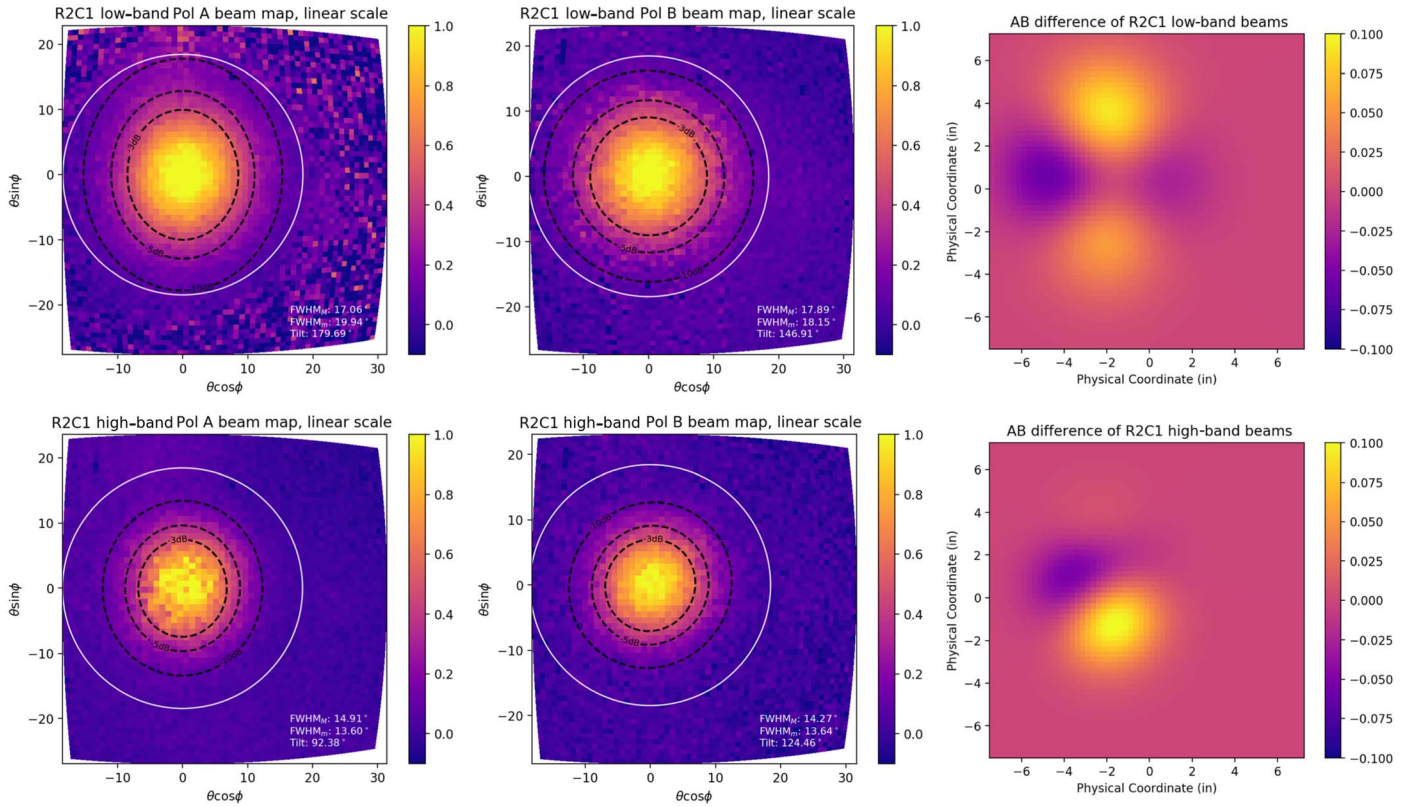

Figure 8. Far-field beam-map measurements of a representative low-band detector pair (upper row) and a high-band detector pair (lower row). These four detectors are low- and high-band A/B polarization pairs from an edge pixel. All plots show the beam map and a 2D Gaussian fit with −3, −5, −10 dB black dashed contour lines overlaid on top. The white line overlays the optical footprint of an $f/1.5$ system. The polarized frame edge affects the Pol. A antennas and causes an ellipticity of the main beam. Pol. B is unaffected by the frame. The 2D Gaussians are differenced in the last column, showing A–B differences. The peak-to-peak differences for the low band are 9% and −6%, and for the high band they are 10% and −5%. This detector shows typical performance. Peak-to-peak variations as low as 10% have been measured on edge pixels; this is near the ∼8% theoretical limit.

mapper facing the detectors with Eccosorb HR-10. Since there are no focusing optics in the testbed cryostat, the chopped source was located in the far field of the detector array.

We demodulate the time-ordered data using the chopper optical encoder as reference, so that only variations at the chop frequency and in phase are interpreted as signal. This reference signal was read out using the same readout electronics employed for the detectors.

Out-of-band photons, rather than being captured by the antennas and filtered out by the on-chip filters, can inadvertently directly illuminate the bolometer island. The exact mechanism for this response is not fully understood, but a plausible mechanism is that it caused by potential differences in the bolometer island relative to the ground plane, which drive currents in the resistive termination and heat the bolometer island (Zhang 2023).

In order to control for the baseline response of the detectors, we measured the direct island response using out-of-band, high-frequency photons. This response is mapped out and subtracted from our nominal beam maps. These data were acquired by filtering the source with a specially designed thick-grill filter, a one cm thick metallic plate with a dense array of circular waveguide apertures. The filter is designed to permit only power above the waveguide cutoff, 61 GHz, allowing illumination solely through direct island stimulation.

Figure 8 shows the resulting beam map, corrected for direct island illumination. Each of the beam maps are fitted to a 2D Gaussian with full width at half maximum (FWHM) in the plot inset and −3, −5, and −10 dB contours plotted on top. We also include the $f/1.5$ optics on top of the beam map. The theoretical expectations for 12×12 pairs of antennas, convolved with the beam of a single element bowtie antenna, match well with the measured results. For a δ-function response at 35 and 45 GHz, we compute an FWHM of 19°.6 and 15°.8, respectively. Real beam maps are an average over the entire band.

In the rightmost panel of Figure 8, we show A–B differences for this representative edge pixel. A simulated finite antenna array, with no edge effects, is expected to have ∼3% peak-to-peak differences in a quadrupole pattern.

Edge effects caused by a solid frame are expected to cause strong differential pointing and result in peak-to-peak variations of 30%–40%, depending on the precise distance between the frame and the antenna array (Soliman 2023). An optimal spacing and corrugated frame is expected to achieve polarized beam residuals of less than 10% from peak to peak. Our measurements show that a representative edge pixel has 15% peak-to-peak beam residuals. This is similar to beam maps from center pixels, suggesting that the polarized beam residuals are not dominated by electromagnetic interactions with the corrugated frame.

4. Conclusion

At any frequency, dichroic detectors offer twice the number of detectors in the same focal plane footprint, allowing a $\sqrt{2}$ improvement in noise-equivalent temperature (NETs). However, at these lower CMB observation frequencies, pixel sizes

must scale accordingly with the wavelengths, resulting in naturally smaller values for N. The NETs show steeper improvement in this regime, and therefore there is a larger absolute benefit from increasing N at these lower frequencies.

We have developed a compact, linearly polarized antenna with a broad first resonance. This first resonance can effectively be divided into two distinct frequency bands, operating at 30/40 GHz.

This antenna is compact and well-suited for integration into BICEP's phased antenna array architecture. The detectors are entirely planar and fully lithographed in thin films without the need for any focusing optics. The top-hat illumination maximizes the directivity of the antenna beam within the smallest area. It exhibits beam characteristics on par with the slot antenna arrays, making it a suitable choice for CMB polarimetry. Overall, the antenna array architecture enables the highest pixel density for a fixed focal plane area.

This detector array deployed in the inaugural season of BICEP Array, and it is the first demonstration of a dichroic planar array system ever used for CMB measurements at the South Pole (Soliman 2023). This work enhances the sensitivity of BICEP array toward low-frequency foregrounds. The dual-frequency measurement enables simultaneous measurement of both the synchrotron amplitude and its spectral index, offering a more powerful constraint on this source of foreground for CMB polarimetry. Further on-sky synchrotron data, recorded by this detector, are being analyzed for a potential publication in the near future.

Immediate future work would be to improve the optical efficiency of the detectors by identifying the source of impedance mismatch in the microstrip summing tree. Furthermore, the potential for higher-frequency focal planes (220–270 GHz) would allow for ever more precise constraints of thermal dust emission. However, the scalability of the current design poses certain challenges. While the antenna elements themselves would scale in proportion to wavelength, the microwave feed network encounters nontrivial scaling issues. The impedance of microstrip lines and desired spacing between these lines may not necessarily decrease with higher frequencies. The existing design, already constrained by space at these frequencies, poses a challenge in scaling down the antenna elements while maintaining similar microstrip trace widths. These challenges have been preliminary addressed in this publication (Soliman 2023) for two CMB observation bands at 90/150 GHz, simultaneously. Additionally, dielectric loss is larger at higher microwave frequencies, leading to expected degradations in performance. These challenges underscore the considerable efforts required in order to extend the design to higher frequencies. Addressing these issues would allow us to place more detectors in the sky; this is especially important at higher frequencies, where detectors are more easily limited by photon background.

Acknowledgments

This research was carried out (in part) at the Jet Propulsion Laboratory, California Institute of Technology, under a contract with the National Aeronautics and Space Administration and funded through JPL's Strategic University Research Partnerships (SURP) program. This publication is also supported by the National Aeronautics and Space Administration grant No. NNX17AC55G.

Appendix A
Improving Diplexer Separation

The diplexer design in Section 2.5 is optimized to minimize reflections in band but exhibits significant spillover between the two bands. The band overlap diminishes our ability to measure the synchrotron SED slope. In a separate fabrication run, we optimized the diplexer for band separation.

We designed a diplexer shown in Figure 9, consisting of two parallel bandpass filters, each centered at 30 and 40 GHz with a 10 GHz bandwidth. The architecture is identical to previously designed bandpasses: a three-pole LC-tank joined with shunt capacitors acting as impedance inverters.

In order to minimize electrical interactions between the two bands, we found it advantageous to have a steep cutoff for the bandpass filters. When the bandpass filter is out of band, the resistance drops to zero and the reactance diverges. A sharper bandpass results in less interaction between the two filters. We found it advantageous to use a diplexer with 0.5 dB ripples or have variations of up to 12% in the passband.

Achieving this steep cutoff required a substantial increase in inductor values. However, achieving these inductor values lithographically would be challenging at our operational frequencies. Instead, we found it advantageous to decrease the diplexer's operating impedance, Z_0, from 25 Ω to 10 Ω to decrease inductor values while keeping the capacitors within achievable values. Additionally, unlike our previous bandpass filter, we did not need to perform a Y-to-π transformation for the capacitive network. Therefore, Figure 9 shows the circuit topography optimized for our design. This is then translated to lithography on the right side of Figure 10.

The measured spectra in Figure 10 show that this diplexer scheme achieves sharper band definitions between the two pixels. However, strong ringing in the passband degrades pixel

	L_1	C_1	L_2	C_2	C_3
Bandpass (30GHz)	3.54	0.78	4.45	0.78	1.14
Bandpass (40GHz)	4.42	0.58	5.35	0.58	1.15

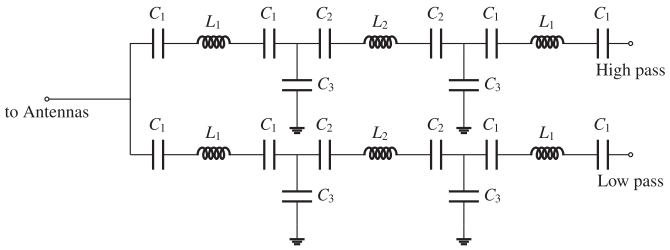

Figure 9. A diplexer composed of two bandpass filters. Each bandpass filter is composed of a three-pole LC resonator circuit. The design table for the circuit network is tabulated on the left. To scale from design table to physical values: inductor values are scaled by $\omega_0^{-1}Z_0$ and capacitor values are scaled by $(\omega_0 Z_0)^{-1}$, where $\omega_0 = 2\pi f_0$ is the desired central frequency of the bandpass filters (30 and 40 GHz), and Z_0 is the port impedance. For this design, $Z_0 = 10\ \Omega$ has been lowered in order to achieve smaller and more physically realizable inductor values. Simulations are then performed to convert the electrical inductance and capacitance to a lithographic element.

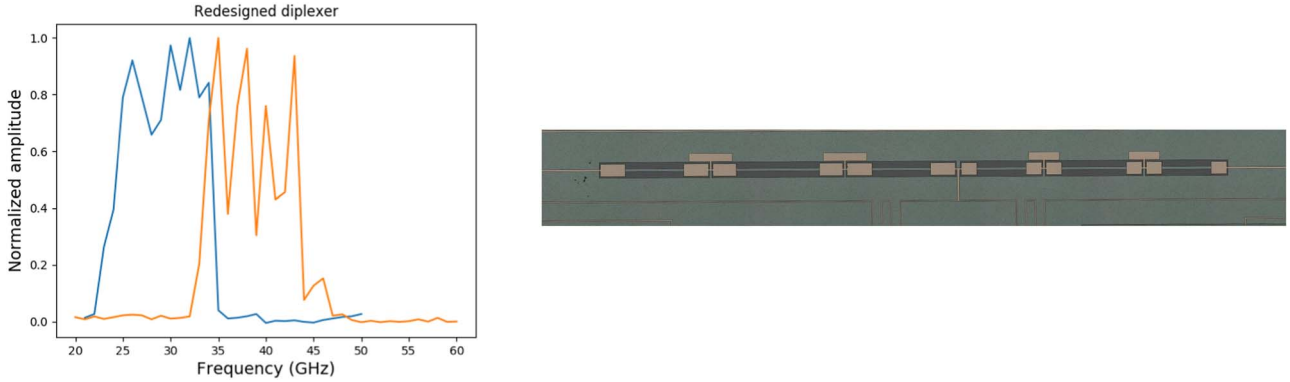

Figure 10. (Left) Measured spectra of the double-bandpass diplexer from a pair of characteristic pixels. We have a stronger band definition between the two bands. However, an impedance mismatch degrades the performance of these pixels. The photograph on the right shows the newly designed diplexer consisting of two bandpass filters. Each bandpass comprises a three-pole series LC resonator circuit joined by shunt capacitors.

performance, resulting in lower optical response. This design requires further investigation to identify the source of the impedance mismatch's source.

Appendix B
Procedure to Convert Lumped Elements to Lithography with Sonnet

This appendix documents our procedure for converting lumped elements into lithographic designs. The fundamental building block of a bandpass filter is the LC resonator, consisting of a series inductor and series capacitor as shown in Figure 11.

The output of a Sonnet simulation is an S-matrix of the two-port network. These can be converted to an impedance matrix:

$$z_{11} = Z_0 \frac{(1+s_{11})(1-s_{22}) + s_{12}s_{21}}{(1-s_{11})(1-s_{22}) - s_{12}s_{21}}, \tag{B1}$$

$$z_{12} = Z_0 \frac{2s_{12}}{(1-s_{11})(1-s_{22}) - s_{12}s_{21}}, \tag{B2}$$

$$z_{21} = Z_0 \frac{2s_{21}}{(1-s_{11})(1-s_{22}) - s_{12}s_{21}}, \tag{B3}$$

$$z_{22} = Z_0 \frac{(1-s_{11})(1+s_{22}) + s_{12}s_{21}}{(1-s_{11})(1-s_{22}) - s_{12}s_{21}}. \tag{B4}$$

The equivalent circuit for the Z-matrix of any reciprocal two-port network is shown in Figure 12. Therefore, a generic series impedance from a two-port network can be calculated by the impedance parameters as demonstrated in Figure 12:

$$Z = \frac{Z_{11}Z_{22} - Z_{12}^2}{Z_{12}}. \tag{B5}$$

Additionally, the circuit model of an LC resonator, shown in Figure 11, has the impedance

$$Z = i\omega L + \frac{2}{i\omega C} = i\left(\omega L - \frac{2}{\omega C}\right). \tag{B6}$$

The derivative of this expression gives us an additional constraint equation:

$$\frac{\partial Z}{\partial f} = 2\pi \frac{\partial Z}{\partial \omega} = \frac{2\pi}{\omega} i\left(\omega L + \frac{2}{\omega C}\right). \tag{B7}$$

These may be expressed as a system of equations:

$$\begin{pmatrix} Z \\ \frac{\omega}{2\pi}\frac{\partial Z}{\partial f} \end{pmatrix} = i \begin{pmatrix} 1 & -2 \\ 1 & 2 \end{pmatrix} \begin{pmatrix} \omega L \\ \frac{1}{\omega C} \end{pmatrix}, \tag{B8}$$

with the corresponding inverse

$$\begin{pmatrix} \omega L \\ \frac{1}{\omega C} \end{pmatrix} = -\frac{i}{2} \begin{pmatrix} 1 & 1 \\ -\frac{1}{2} & \frac{1}{2} \end{pmatrix} \begin{pmatrix} Z \\ \frac{\omega}{2\pi}\frac{\partial Z}{\partial f} \end{pmatrix}. \tag{B9}$$

This allows us to solve for the inductance and capacitance, where Z determined by Equation (B5):

$$L = \frac{1}{2\omega}\left(Im[Z] + \frac{\omega}{2\pi} Im\left[\frac{\partial Z}{\partial f}\right]\right), \tag{B10}$$

$$C = \frac{1}{4\omega}\left(-Im[Z] + \frac{\omega}{2\pi} Im\left[\frac{\partial Z}{\partial f}\right]\right)^{-1}. \tag{B11}$$

Additionally, the parasitic capacitance is

$$C_p = \frac{1}{i\omega}\frac{Z_{22} - Z_{11}}{Z_{11}Z_{22} - Z_{12}^2} = \frac{1}{\omega}\frac{Im[Z_{22}] - Im[Z_{11}]}{Z_{11}Z_{22} - Z_{12}^2}. \tag{B12}$$

To develop a lithographed filter, we first compile a comprehensive library of LC resonator simulations for a fixed dielectric stack. We use the niobium metal model in Sonnet, which has zero resistance in DC and AC and accounts for kinetic inductance with $L_s = 0.11$ pH/sq. We conduct simulations with various lengths of capacitors and inductors, systematically tabulating the lumped-element equivalent models, including the frequency dispersions of both elements. Subsequently, when aiming for a specific lumped-element model, we interpolate the precise geometric parameters necessary for achieving the desired filter characteristics. Then, a realized lithographic filter is fully simulated and tweaked if necessary. This iterative process allows us to fine-tune and optimize the lithographic design to meet specific performance criteria and minimize frequency dispersion.

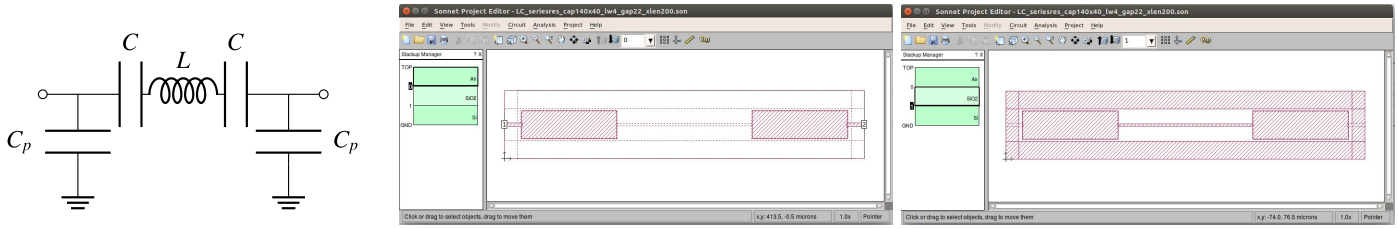

Figure 11. The leftmost figure shows a circuit model equivalent to the LC resonator shown in the two figures on the right: a series LC resonator with parasitic capacitances to ground. The middle image shows the Sonnet simulation from the top microstrip trace layer, and the rightmost image shows the Sonnet simulation from the ground-plane layer.

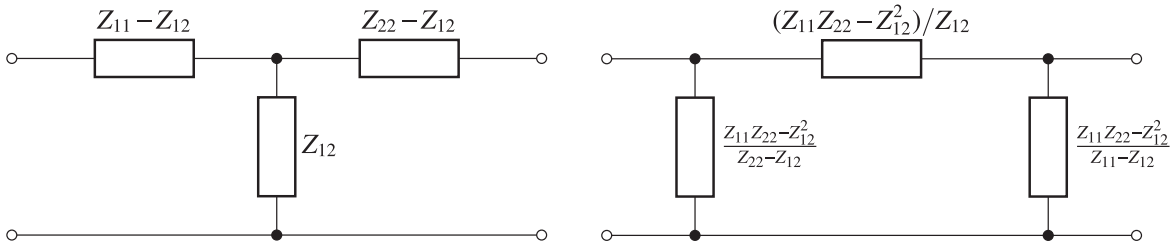

Figure 12. (Left) A generic two-port representation with impedance parameters. (Right) An equivalent representation.

Appendix C
Aperture Efficiencies of Antenna Arrays

Aperture efficiency is a measure of how effectively an optical system captures and utilizes incoming radiation. For an extended source like the CMB, aperture efficiency is determined entirely by the spillover efficiency, ϵ_s (Goldsmith 1998):

$$\epsilon_{\text{aperture efficiency}} = \epsilon_s. \tag{C1}$$

In this section, we assume the antenna array consists of an isotropic radiator, $G_0(\theta, \phi) = 1$, constructing the array beam entirely through the array factor. For a simple lens system with $f/\#$, the field of view extends between 0 and $\theta_0 = \arctan((2f/\#)^{-1})$. Consequently, the spillover efficiency represents the fractional power contained within a specified field of view:

$$\epsilon_s = \frac{\int_0^{2\pi} d\phi \int_0^{\theta_0} d\theta \ |AF(\theta, \phi)|^2 \sin\theta}{\int_0^{2\pi} d\phi \int_0^{\pi/2} d\theta \ |AF(\theta, \phi)|^2 \sin\theta}, \tag{C2}$$

where $AF(\theta, \phi)$ is the array factor and $|AF|^2$ is the radiation pattern of the antenna system.

In Figure 13, we analyze aperture efficiency by varying the antenna array size and tapering. A small antenna array, $<0.5F\lambda$, would not be very directive, resulting in low spillover efficiency. As the number of antenna elements increases, the directivity increases, and the spillover efficiency increases as well. Large antenna arrays $>2F\lambda$ will be very directive and approach the point of having no spillover, at the cost of being physically larger.

Furthermore, a Gaussian edge taper reduces side-lobe levels, enhancing peak spillover efficiencies. However, aggressive edge tapering requires larger pixels, which conflicts with dense packing of pixels.

Following the prescription in Section 4.2 of Griffin et al. (2002), we can compare the relative mapping speed of different detector focal planes for an extended source. The power as seen by a detector in the Rayleigh–Jeans limit has the form

$$P = \eta_0 \eta_s A\Omega \left(\epsilon \frac{k_b T}{\lambda^2}\right) \Delta\nu, \tag{C3}$$

where η_0 is the detector optical efficiency, η_s is the spillover efficiency, $A\Omega$ is the detector throughput, ϵ is the emissivity of a source at temperature T, and $\Delta\nu$ is the bandwidth of the detector. The fundamental noise sources include the photon noise and intrinsic detector noise,

$$NEP^2 = NEP_\gamma^2 + NEP_{\text{detector}}^2 = NEP_\gamma^2(1 + \gamma^2), \tag{C4}$$

where we parameterize $\gamma = \frac{NEP_{\text{detector}}}{NEP_\gamma}$ as the ratio of detector noise to photon noise. Commonly, these detectors are in the photon-noise limit, so $\gamma < 1$. We can then make an approximation that the bunching noise term is subdominant to the Poisson noise term:

$$NEP^2 \approx 2\hbar\nu_0 P(1 + \gamma^2). \tag{C5}$$

The corresponding single-detector NET is then

$$NET = \frac{NEP}{\frac{\partial P}{\partial T}} = \frac{2\hbar\nu_0}{\sqrt{\eta_0\eta_s A\Omega\left(\epsilon \frac{k_b}{\lambda^2}\right)\Delta\nu}} \sqrt{1 + \gamma^2}, \tag{C6}$$

A focal plane NET allows us to compare the relative mapping speeds of two different focal planes when observing the same source. The relative instantaneous sensitivities of the two focal planes are expressed as

$$\frac{NET}{NET'} = \sqrt{\frac{(N\eta_0\eta_s A\Omega\Delta\nu)'}{N\eta_0\eta_s A\Omega\Delta\nu}} \sqrt{\frac{1 + \gamma^2}{1 + \gamma'^2}}. \tag{C7}$$

Therefore, the relative mapping speed of a single-moded, photon-noise limited detector array depends on the number of detectors, optical efficiency, spillover efficiency, and total bandwidth. Consequently, optimizing an array naturally strikes a balance between a dense pixel packing size, $\sim 1.5F\lambda$, with maximizing spillover efficiency and optical

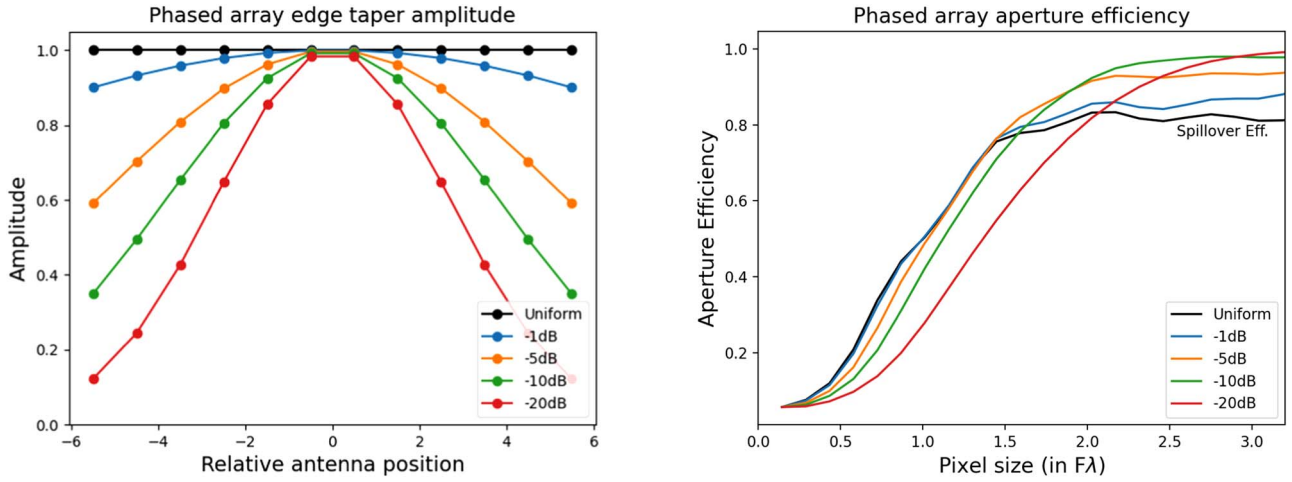

Figure 13. (Left) Illumination of an example 12 element antenna array with different edge tapers. (Right) Calculation of the aperture efficiency of an $N \times N$ antenna array with different edge tapers. The dashed lines show a uniformly illuminated array's illumination and spillover efficiencies. The antenna array presented in this publication is uniformly illuminated with a pixel size of $\sim$1.5, $2.0F\lambda$ for the two bands, respectively.

efficiency. Additionally, in the limit that the photon-noise contribution comes from the bunching term, the relative mapping speed only depends on the square root of the number of detectors and their bandwidth.

The calculations presented here apply directly to other single-mode optical systems like horn-coupled detectors. A horn-coupled antenna's edge taper varies depending on the specific details of the horn profile, complicating cross-comparisons between these two optical architectures. Nevertheless, antenna arrays offer a straightforward means of controlling the degree of taper. This allows them to excel in achieving a tightly controlled illumination pattern and offering the highest pixel density.

ORCID iDs

Corwin Shiu https://orcid.org/0000-0002-6635-5950
William C. Jones https://orcid.org/0000-0002-3636-1241
Lorenzo Moncelsi https://orcid.org/0000-0002-4242-3015
Cheng Zhang https://orcid.org/0000-0001-8288-5823

References

Ade, P. A. R., Pisano, G., Tucker, C., & Weaver, S. 2006, Proc. SPIE, 6275, 62750U
Ade, P. A. R., Ahmed, Z., Aikin, R. W., et al. 2016, ApJ, 833, 228
Ade, P. A. R., Ahmed, Z., Aikin, R. W., et al. 2019, ApJ, 884, 114
Ade, P. A. R., Ahmed, Z., Amiri, M., et al. 2021, PhRvL, 127, 151301
Ade, P. A. R., Aikin, R. W., Amiri, M., et al. 2014, ApJ, 792, 62
Ade, P. A. R., Aikin, R. W., Barkats, D., et al. 2015, ApJ, 814, 110
Arbabi, A., Boutejdar, A., Mahmoudi, M., & Omar, A. 2006, in 2006 First Int. Conf. on Communications and Electronics (Piscataway, NJ: IEEE), 478
Balanis, C. A. 2016, Antenna Theory: Analysis and Design (4th ed.; New York: John Wiley & Sons)
Bennett, C. L., Larson, D., Weiland, J. L., et al. 2013, ApJS, 208, 20
Benson, B. A., Ade, P. A. R., Ahmed, Z., et al. 2014, Proc. SPIE, 9153, 91531P
BICEP2 Collaboration, Keck Array Collaboration, SPIDER Collaboration, et al. 2015, ApJ, 812, 176
Brandt, W. N., Lawrence, C. R., Readhead, A. C. S., Pakianathan, J. N., & Fiola, T. M. 1994, ApJ, 424, 1
Brown, G., & Woodward, O. 1952, RCARv, 13, 425
Choi, S. K., & Page, L. A. 2015, JCAP, 2015, 020
Chu, L. 1948, JAP, 19, 1163
de Korte, P. A. J., Beyer, J., Deiker, S., et al. 2003, RScI, 74, 3807
Dobbs, M. A., Lueker, M., Aird, K. A., et al. 2012, RScI, 83, 073113
Draine, B. T., & Hensley, B. 2013, ApJ, 765, 159
Draine, B. T., & Lazarian, A. 1999, ApJ, 512, 740
Eimer, J. R., Li, Y., Brewer, M. K., et al. 2024, ApJ, 963, 92
Finkbeiner, D. P., Davis, M., & Schlegel, D. J. 1999, ApJ, 524, 867
Ginzburg, V. L. 1969, CoASP, 1, 49
Goldsmith, P. F. 1998, Quasioptical Systems: Gaussian Beam Quasioptical Propagation and Applications (1st ed.; Wiley-IEEE Press: New York)
Griffin, M. J., Bock, J. J., & Gear, W. K. 2002, ApOpt, 41, 6543
Herman, D., Hensley, B., Andersen, K. J., et al. 2023, A&A, 675, A15
Hoang, T., & Lazarian, A. 2016, ApJ, 821, 91
Hu, W., Hedman, M. M., & Zaldarriaga, M. 2003, PhRvD, 67, 043004
Hui, H., Ade, P. A. R., Ahmed, Z., et al. 2018, Proc. SPIE, 10708, 1070807
Irwin, K., & Hilton, G. 2005, in Transition-Edge Sensors, ed. C. Enss (Berlin: Springer), 63
Irwin, K. D., & Lehnert, K. W. 2004, ApPhL, 85, 2107
Kamionkowski, M., & Jaffe, A. H. 2001, IJMPA, 16, 116
Kiuchi, K., Adachi, S., Ali, A. M., et al. 2020, Proc. SPIE, 11445, 114457L
Kogut, A., Dunkley, J., Bennett, C. L., et al. 2007, ApJ, 665, 355
Krachmalnicoff, N., Carretti, E., Baccigalupi, C., et al. 2018, A&A, 618, A166
Kuo, C. L., Bock, J. J., Bonetti, J. A., et al. 2008, Proc. SPIE, 7020, 70201I
Mather, J. C. 1982, ApOpt, 21, 1125
Matthaei, G. L., & Jones, L. Y 1980, Microwave Filters, Impedance-Matching Networks, and Coupling Structures (Dedham, MA: Artech House Books)
McMahon, J., Beall, J., Becker, D., et al. 2012, JLTP, 167, 879
Mushiake, Y. 1992, IAPM, 34, 23
O'Brient, R., Ade, P., Arnold, K., et al. 2010, Proc. SPIE, 7741, 77410J
O'Brient, R., Ade, P., Arnold, K., et al. 2013, ApPhL, 102, 063506
O'Brient, R., Ade, P. A. R., Ahmed, Z., et al. 2012, Proc. SPIE, 8452, 84521G
O'Brient, R., Edwards, J., Arnold, K., et al. 2008, Proc. SPIE, 7020, 70201H
Page, L., Hinshaw, G., Komatsu, E., et al. 2007, ApJS, 170, 335
Planck Collaboration, Ade, P. A. R., Aghanim, N., et al. 2016, A&A, 594, A25
Planck Collaboration, Akrami, Y., Ashdown, M., et al. 2020, A&A, 641, A11
Pozar, D. M. 2005, Microwave Engineering (3rd ed.; Hoboken, NJ: Wiley)
Qu, S.-W., & Ruan, C.-L. 2006, Prog. Electromagn. Res., 57, 179
Schillaci, A., Ade, P. A. R., Ahmed, Z., et al. 2023, JLTP, 213, 317
Seljak, U., & Zaldarriaga, M. 1997, PhRvL, 78, 2054
Soliman, A. 2023, PhD thesis, California Institute of Technology
Soliman, A., Ade, P. A. R., Ahmed, Z., et al. 2020, JLTP, 199, 1118
Stutzman, W. L., & Thiele, G. A. 2012, Antenna Theory and Design (3rd ed.; New York: John Wiley & Sons)
Suzuki, A., Ade, P., Akiba, Y., et al. 2016, JLTP, 184, 805
Thornton, R. J., Ade, P. A. R., Aiola, S., et al. 2016, ApJS, 227, 21
Tretyakov, M., Koshelev, M., Dorovskikh, V., Makarov, D., & Rosenkranz, P. 2005, JMoSp, 231, 1
Walker, S., Sierra, C. E., Austermann, J. E., et al. 2020, JLTP, 199, 891
Zhang, C. 2023, PhD thesis, California Institute of Technology
Zheng, C., Ade, P. A. R., Ahmed, Z., et al. 2020, JLTP, 199, 968
Zmuidzinas, J. 2003, ApOpt, 42, 4989